NANO LETTERS

Letter

pubs.acs.org/NanoLett

Extraordinary Room-Temperature Photoluminescence in Triangular WS_2 Monolayers

Humberto R. Gutiérrez,[†,∥] Nestor Perea-López,[†] Ana Laura Elías,[†] Ayse Berkdemir,[†] Bei Wang,[†] Ruitao Lv,[†] Florentino López-Urías,[†,⊥] Vincent H. Crespi,[†] Humberto Terrones,[†] and Mauricio Terrones*[,†,§]

[†]Department of Physics, The Pennsylvania State University, University Park, Pennsylvania 16802, United States

[§]Department of Materials Science and Engineering and Materials Research Institute, The Pennsylvania State University, 104 Davey Lab., University Park, Pennsylvania 16802, United States

Supporting Information

ABSTRACT: Individual monolayers of metal dichalcogenides are atomically thin two-dimensional crystals with attractive physical properties different from those of their bulk counterparts. Here we describe the direct synthesis of WS_2 monolayers with triangular morphologies and strong room-temperature photoluminescence (PL). The Raman response as well as the luminescence as a function of the number of S−W−S layers is also reported. The PL weakens with increasing number of layers due to a transition from direct band gap in a monolayer to indirect gap in multilayers. The edges of WS_2 monolayers exhibit PL signals with extraordinary intensity, around 25 times stronger than that at the platelet's center. The structure and chemical composition of the platelet edges appear to be critical for PL enhancement.

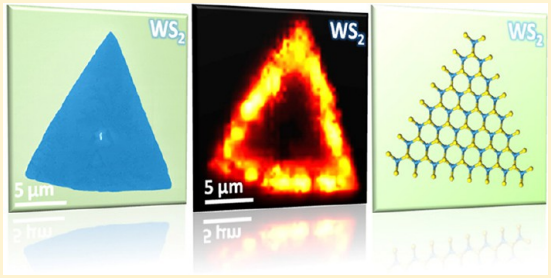

KEYWORDS: *Metal dichalcogenides, tungsten disulfide, 2D materials, photoluminescence, Raman*

The synthesis and isolation of atomically thin two-dimensional (2D) crystals such as graphene[1] and boron nitride[2,3] have enabled fascinating advances in 2D metallic (graphene) and insulating (h-BN) systems.[4−6] However, many potential applications require intermediate behavior, that is, semiconductors. In this context, monolayers of transition metal dichalcogenides such as MoS_2 and WS_2, have recently caught the attention of the scientific community as 2D semiconductor crystals with direct gaps in the visible spectrum;[7−12] in bulk form these systems have indirect band gaps. The bulk transition metal disulfides exhibit strong intralayer sulfur−metal covalent bonds (with metal atoms sandwiched by sulfur layers) and weak interlayer van der Waals stacking. The isolation of single atomic layers from these materials has been an experimental challenge due to the material's natural tendency to form closed fullerene-like,[13−16] nanotube,[17,18] or stacked multilayered[17] geometries. Few-layer MoS_2 has been successfully synthesized by annealing $(NH_4)_2MoS_4$ thin films.[19] Recently, MoS_2 monolayers have been isolated via mechanical exfoliation,[7,8,20] wet chemical approaches,[9,21,22] physical vapor deposition,[23] and sulfurization of molybdenum films;[24,25] their electronic and optical properties include carrier mobilities of ∼200 $cm^2\ V^{-1}\ s^{-1}$ and weak room-temperature photoluminescence.[7−9,20,26,27] In contrast, WS_2 monolayers have only been prepared by chemical routes, and their characterization was limited to structural studies[21,22] and band structure calculations.[10−12]

Here we report the synthesis of single- and few-layered 2D triangular microplatelets of WS_2 via the sulfurization of ultrathin WO_3 films. These 2D islands displayed extraordinarily strong photoluminescence (PL) from their edges, at room temperature and visible wavelengths. A combination of Raman spectroscopy, atomic force microscopy (AFM), and scanning and high-resolution transmission electron microscopy (SEM, HRTEM) confirmed that the samples indeed consist of a single S−W−S layer and revealed that the giant PL signal arises from the vicinity of edges with zigzag termination. Our first-principles density functional theory (DFT) calculations show that the system becomes direct gap upon thinning to a single layer, consistent with the experimental observation of strong PL only in single-layer platelets.

The 2H-WS_2 polytype crystalline structure has the hexagonal space group $P6_3/mmc$ with lattice parameters of a = 3.1532 Å and c = 12.323 Å.[28] Each WS_2 monolayer contains a single layer of W atoms with a 6-fold coordination symmetry, hexagonally packed between two trigonal atomic layers of S atoms, as depicted in Figure 1a,b. Similar to MoS_2, bulk WS_2 is an indirect-gap semiconductor; it has a gap of 1.3 eV.[14,29] However, theoretical calculations reveal that with decreasing number of layers, WS_2 transitions from indirect gap (in bulk) to

Received: July 17, 2012
Revised: November 9, 2012
Published: November 29, 2012

dx.doi.org/10.1021/nl3026357 | *Nano Lett.* 2013, 13, 3447−3454

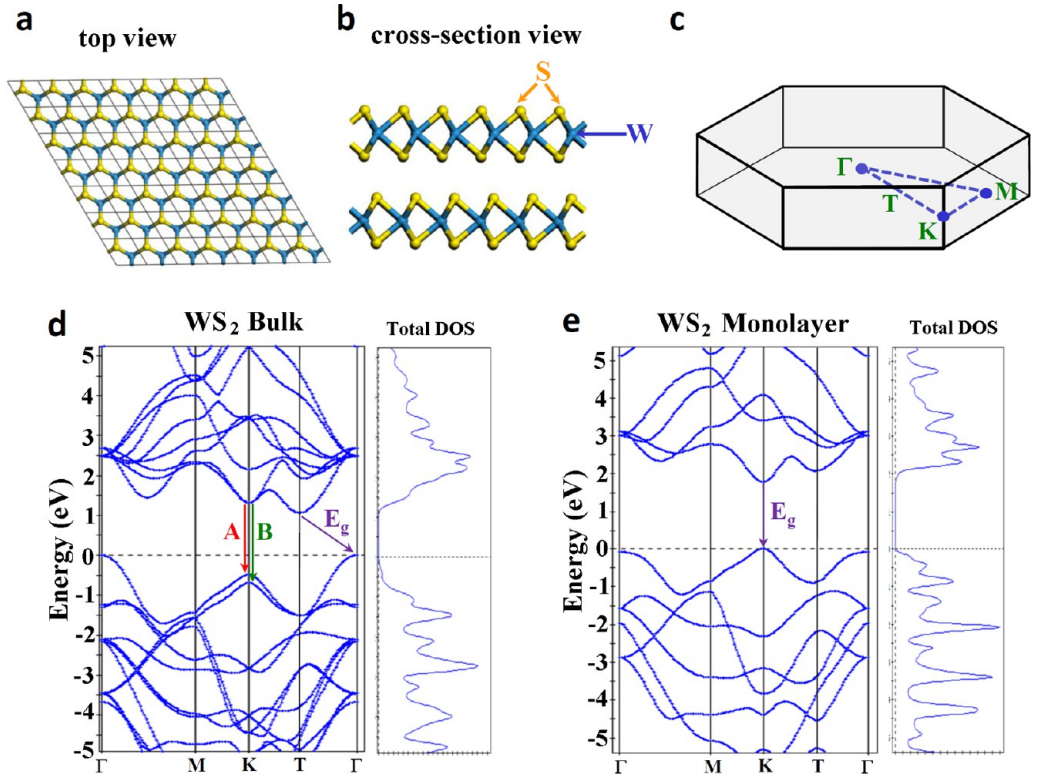

Figure 1. (a and b) top and cross-section view of the WS_2 atomic structure. (c) Brillouin zone for WS_2 monolayer. (d, e) Electronic band structure (left) and total density of states (right) for the WS_2 bulk and monolayer, respectively.

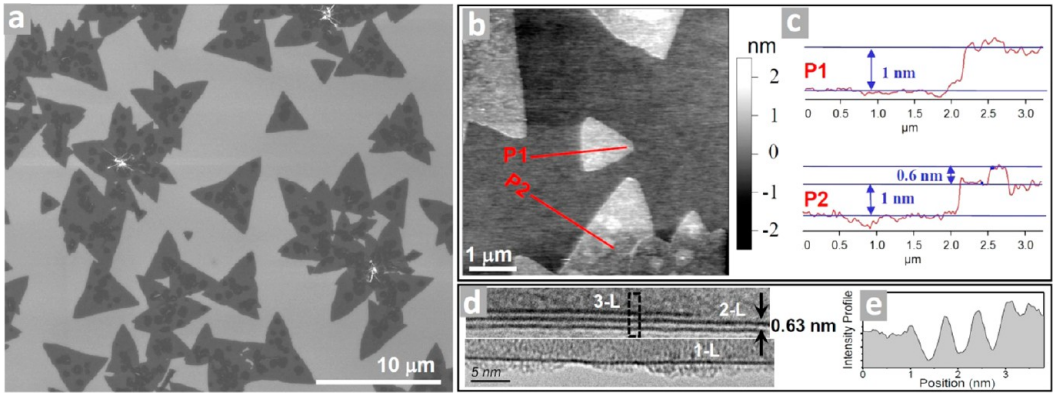

Figure 2. (a) SEM image of small triangular 2D clusters of WS_2 monolayer; the dark contrast spots in the interior of the islands are second-layer clusters in an early stage of growth. (b, c) AFM image and height profiles along two different directions (P1 and P2) revealing the positions of one and two WS_2 layers. (d) Cross-section TEM images of clusters containing 3L, 2L (top), and 1L (bottom); the plot in part (e) corresponds to the intensity profile of the region enclosed by the dashed box in part d. The spacing between WS_2 layers is in agreement with the AFM measurements.

direct gap (in a monolayer),[11] as shown in Figure 1d and e (see Supporting Information for computational details). For bulk WS_2, the electronic states involved in the indirect transition (i.e., the valence band maximum at Γ and the conduction band minimum at T) originate from linear combinations of tungsten d-orbitals and sulfur p_z-orbitals. These electronic states exhibit a strong interlayer coupling, and their dispersion strongly depends on the number of layers. For a monolayer, the indirect gap between these states is larger than the direct transition at K, thus making the material a direct band gap semiconductor (Figure 1d and e). The conduction and valence states at K are mainly due to tungsten d-orbitals, and their energies are not very sensitive to the number of layers; the experimental direct band gap at the K point is ~2.05 eV.[14,29] However, small differences between the valence band at K between bulk and monolayer are noteworthy. In the bulk, there are two well-known direct transitions at the K point due to the splitting of the valence band; experimentally these transitions have been observed by absorption spectroscopy[14,30] and assigned as excitons A (1.95 eV)[14,29] and B (2.36 eV)[14,29] (Figure 1d). However, for a monolayer this splitting is absent (see Figure 1e), and only one direct electronic transition is expected to be observed by optical spectroscopy.[30]

One of the most common approaches used to produce WS_2 nanotubes, fullerene-like structures, and films is the sulfurization of WO_3 powders.[31] We have modified this process to yield single- and few-layered symmetric triangular WS_2 clusters of various sizes. First, we deposit ultrathin films (5−20 Å) of WO_3

dx.doi.org/10.1021/nl3026357 | Nano Lett. 2013, 13, 3447−3454

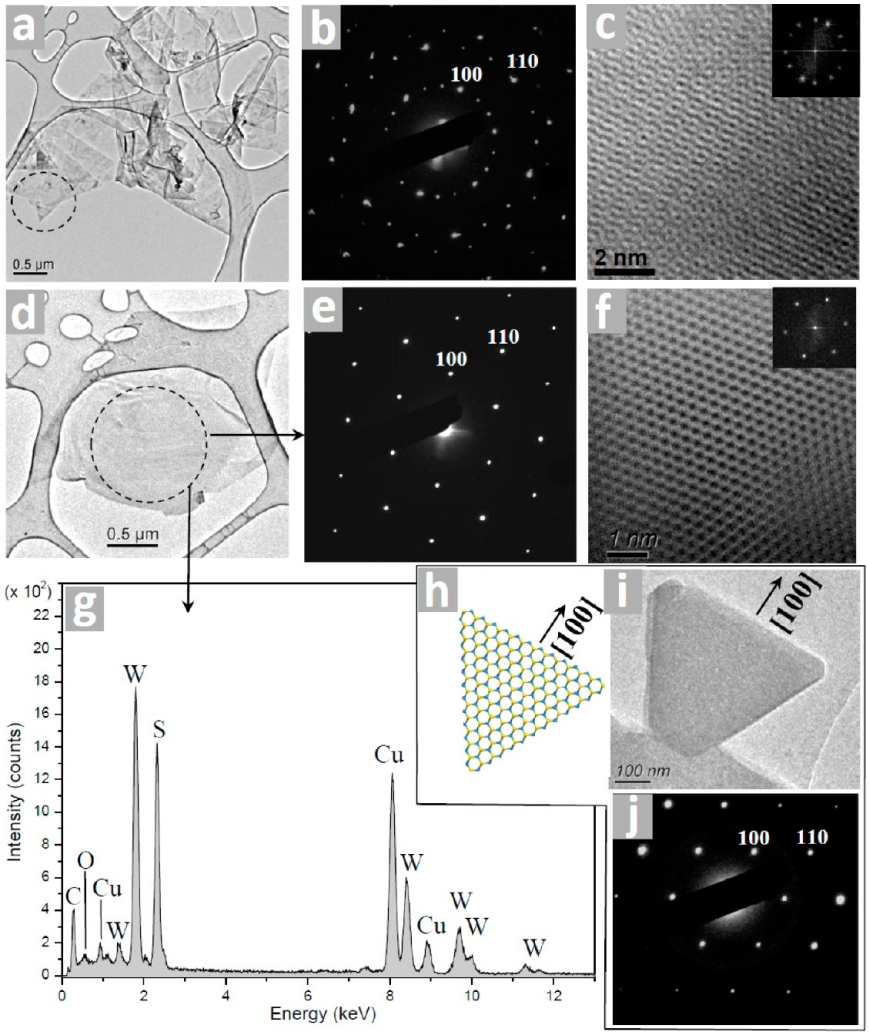

Figure 3. (a, b, and c) Low magnification TEM, electron diffraction pattern, and HRTEM phase-contrast image, respectively, of a WS_2 2D island folded during the transfer. (d, e, and f) TEM, EDP, and HRTEM, respectively, for a single-domain 2D WS_2 crystal. (g) EDS spectrum from the region enclosed by the dashed circle of d. (h, i, and j) Atomic model, TEM image, and EDP, respectively, of a triangular cluster showing that the edges are perpendicular to the [100] direction (zigzag edges).

on a SiO_2/Si substrate by thermal evaporation of WO_3 powder under high vacuum. These films are then exposed to a sulfur-rich atmosphere in a quartz tube reactor at ~800 °C. The thinnest WO_3 films (5−10 Å) produce triangular islands that correspond to an initial stage in the growth of a WS_2 monolayer. Figure 2a provides an SEM image of monolayer triangular islands; the regions with greater contrast in the island interiors indicate the nucleation of a second layer. The film thickness was determined by AFM in noncontact mode (for as-grown samples on SiO_2, Figure 2b,c) and by HRTEM cross-sectional images (for samples transferred to TEM grids, Figure 2d). The typical height measured by AFM for a WS_2 monolayer on SiO_2 was ~1 nm, while the spacing between the first and the second WS_2 monolayers was ~0.6 nm. The ~0.6 nm spacing between WS_2 monolayers is in good agreement with the theoretical value and that obtained by TEM and X-ray bulk diffraction.[28] The larger AFM-derived spacing between the first monolayer and the substrate is not surprising, since it involves distinct tip-sample and sample-substrate interactions; similar effects have been observed for MoS_2[9] and graphene.[32] WS_2 islands ranging from nanometers to micrometers in lateral extent coexist in our samples; we believe that the smallest monolayer islands correspond to the earliest stages of growth. The 2D islands may nucleate by sulfurization of small WO_3 clusters and then expand laterally as W and S species diffuse on the substrate toward the expanding clusters. Lateral growth could eventually result in the coalescence of neighboring WS_2 islands of different crystalline orientation, thus yielding to a large variety of island morphologies.

Electron diffraction studies from platelets transferred onto TEM grids reveal single-crystal domains larger than a micrometer (Figure 3d−f). After transferring the WS_2 islands to the TEM grid, we observe skew-stacked and folded WS_2 layers (Figure 3a), as indicated in the diffraction patterns of Figure 3b. HRTEM images from these regions exhibit the expected Moiré patterns (Figure 3c). High-resolution phase-contrast images from a single-crystal WS_2 monolayer (Figure 3f) reveal the honeycomb-like structure of the plain view projection. Electron diffraction of small triangular islands confirmed that they are single crystals with edges perpendicular to the [100] crystalline direction, suggesting that the islands have mostly zigzag edges (Figure 1h−j). Notice that due to edge roughness a small fraction of the edge could have other orientations. Ideal armchair terminations would alternate S and

dx.doi.org/10.1021/nl3026357 | *Nano Lett.* 2013, 13, 3447−3454

W atoms, whereas ideal zigzag edges can be terminated by a pure element: either S or W. From a chemical standpoint, sulfur is more likely to be on the edges of metal dichalcogenide clusters, as previously demonstrated by scanning tunneling microscopy (STM) of triangular MoS_2 crystals[23] and density functional theory calculations on WS_2 clusters.[33] Detailed calculations suggest that the energetically preferred termination at high sulfur availability is a tungsten-terminated crystallographic zigzag edge, capped by two additional sulfur atoms per edge tungsten. The presence of intense W and S peaks in energy-dispersive X-ray spectroscopy data (Figure 3g) with only a minute amount of O, demonstrate that the WO_x films are efficiently sulfurized and fully converted into WS_2.

Room-temperature Raman spectra of monolayer WS_2 platelets (Figure 4a) show E^1_{2g} and A_{1g} phonon modes at 356 and 417.5 cm^{-1}, respectively. These values are slightly different from those of bulk WS_2 (355.5 and 420.5 cm^{-1}, respectively). Figure 4b shows the thickness dependence of the frequency for the E^1_{2g} and A_{1g} Raman modes. The A_{1g} mode redshifts with decreasing number of layers. The van der Waals interaction between layers in bulk transition metal dichalcogenides stiffens the lattice, which is consistent with softening of the A_{1g} mode in the monolayer. The E^1_{2g} phonon mode, on the other hand, blueshifts for a decreasing number of layers. Similar anomalous behavior of the E^1_{2g} mode has been previously reported in few-layered MoS_2 films[20] and might be caused by stronger dielectric screening of the long-range Coulomb interactions between the effective charges in thicker samples.[34] The frequency difference between these two modes increases with the number of S−W−S layers in the film (Figure 4b).

As discussed earlier, WS_2 is expected to transition from an indirect-gap semiconductor in a multilayered form to a direct-gap semiconductor in a monolayer form. Experimental evidence of this behavior has not previously been reported for the WS_2 system. Our PL experiments shown in Figure 4c give clear evidence of this transition. For a monolayer, the PL is very intense and exhibits a single peak (Figure 4c) corresponding to the direct excitonic transition at the K point (Figure 1e). For increasing number of layers, the indirect transition between the local minimum of the conduction band at the T point and the local maximum of the valence band at the Γ point decreases in energy; hence the indirect transition between these two electronic states starts to compete with the direct transition at the K point (Figure 1d). There is also a valence band splitting at the K point, which generates two distinct excitons (A and B, as labeled in Figure 1d). The competition between direct and indirect electronic transitions dramatically reduces the PL quantum efficiency and gives rise to a new feature at longer wavelength (labeled I in Figure 4c) when the WS_2 film thickness increases to two (2L) or three (3L) layers. The luminescence from exciton B is also apparent for 2L and 3L. Notice that the indirect transition for 2L is higher in energy than that for the 3L and bulk films, suggesting that the 2L electronic bands have not completely evolve to the bulk configuration. The PL from bulk samples is very weak and only shows the features (I) associated with the indirect transition.

We now analyze the Raman and PL as a function of the position on the triangular WS_2 islands. For the 488 nm laser excitation, the intensity of the A_{1g} Raman mode (relative to that of the Si substrate peak) monotonically decreases with decreasing the number of WS_2 layers. Figure 5a and b show SEM images of two different samples, one containing small (~5 μm size) triangular WS_2 islands (Figure 5a) with various

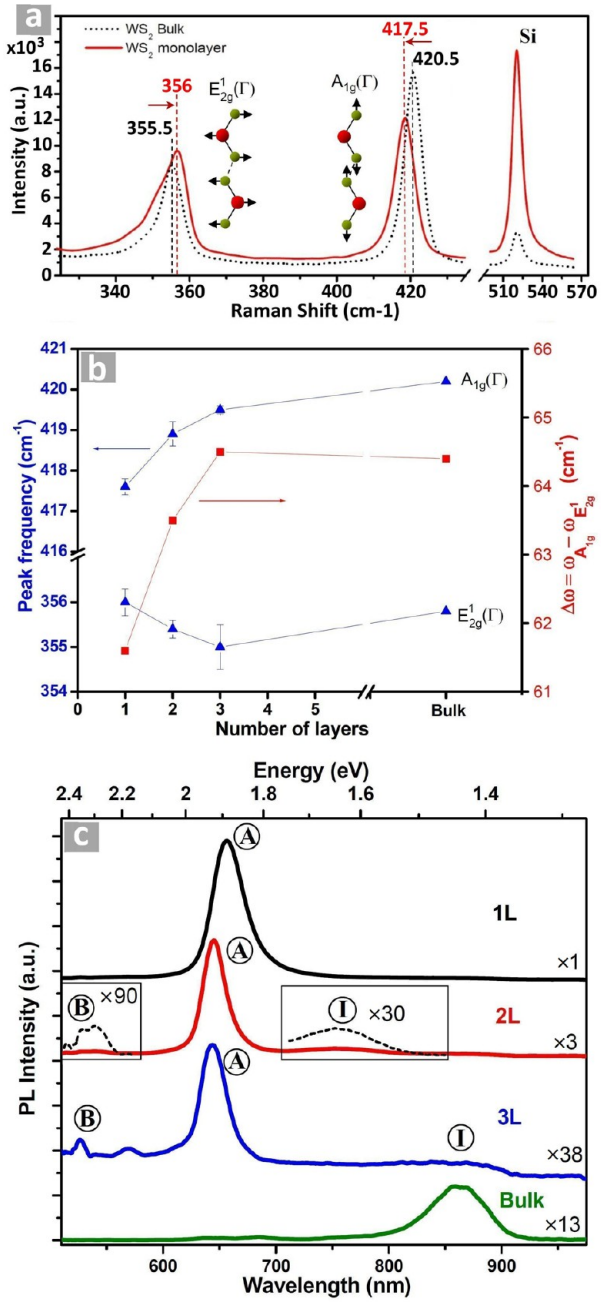

Figure 4. (a) Raman spectra for WS_2 bulk (dotted) and a monolayer (solid red). (b) Frequencies of the E^1_{2g} and A_{1g} Raman modes (blue) and the difference in peak position $\Delta\omega$ (red) as a function of number of WS_2 layers for the 488 nm excitation laser line. (c) Photoluminescence intensities for 1L, 2L, 3L, and bulk using the 488 nm excitation laser line. The positions for the excitons A and B as well as the indirect band gap (I) are labeled.

second- and few-layer plateaus on their surfaces (darker contrast regions), and the other (Figure 5b) having a larger monolayer WS_2 island (~15 μm size) with only two small higher plateaus near the center. The Raman mappings of the intensity ratio $I_{A_{1g}}/I_{Si}$ for those islands are shown in Figure 5c and 5d. The blue region with $I_{A_{1g}}/I_{Si} \sim 0.5$ corresponds to the monolayer part of the islands; this was also confirmed from the frequency shifts of the E^1_{2g} and A_{1g} phonon modes. The Raman mappings enable one to correlate other properties such as the

dx.doi.org/10.1021/nl3026357 | Nano Lett. 2013, 13, 3447−3454

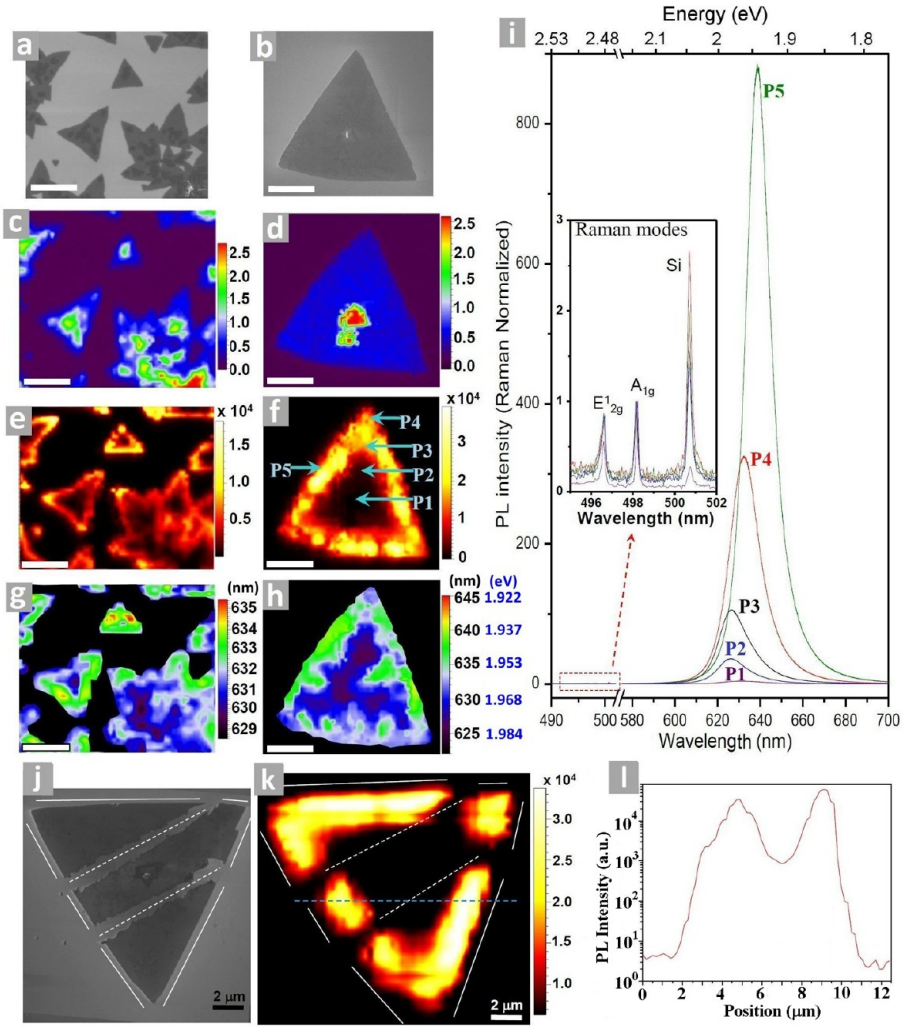

Figure 5. (a, b) SEM images of small and large islands, respectively. (c, d) Raman mappings of the intensity ratio $I_{A_{1g}}/I_{Si}$ corresponding to the islands in a and b, respectively. The region in blue corresponds to a monolayer of WS_2. (e, f) Corresponding PL mappings (absolute maximum intensity of the PL peak). (g, h) Mappings of the PL peak spectral position. The scale bars in a–h are 5 μm. (i) Room-temperature PL spectra at the different positions in the island indicated by arrows in f; the PL intensity was normalized to the intensity of the A_{1g} phonon mode ($I_{A_{1g}}$). The inset is a zoom of the Raman peaks. (j) SEM image of a mechanically scratched island (mechanical scratches are along the dashed lines) and its corresponding PL map (k). The "new" edges created mechanically do not exhibit PL enhancement. (l) PL intensity profile along the dashed horizontal blue line, demonstrating that even at the center of the island there is PL but in less intensity than that obtained close to the edges (notice that the PL intensity scale is logarithmic).

PL response to the location and number of layers in the 2D island.

Figure 5e and f show the spatial distribution of the maximum PL intensity when the excitation laser is scanned over the sample surface. The correlation of PL and Raman maps with the SEM images demonstrates that the extraordinary PL signal arises mainly from monolayers of WS_2. Regions with more than one layer (e.g., P1) exhibit very weak or no PL near ~1.95 eV, consistent with the indirect band gap of few-layer and bulk WS_2. Figure 5i shows the PL spectra obtained from five different positions within the large WS_2 islands of Figure 5b. For this excitation wavelength (488 nm), the A_{1g} Raman peak intensity decreases with the amount of WS_2 material, and both Raman and PL intensity are also equally affected by external factors such as the local electric fields and the laser excitation power;[8] thus we report the PL intensity normalized to the A_{1g} Raman peak intensity. Other than the Raman peaks, a single sharp PL peak (full width at half-maximum of ~42–68 meV) is the only feature observed from 490 to 900 nm. The presence of this single PL peak is in agreement with the theoretical prediction that only one direct electronic transition at the K point should be observed for a WS_2 monolayer (Figure 1a). Direct electronic transitions in WS_2 originate from excitonic radiative relaxation,[14,30,31] and for this reason the PL signal always appears at energies slightly lower than the 2.05 eV direct band gap of WS_2. The position of the PL maximum varies for different locations on the island, between 1.99 and 1.94 eV. Since the Raman frequencies—which are strain-sensitive—are homogeneous across the entire monolayer region of the sample, we rule out inhomogeneous strain as a possible cause for the inhomogeneous exciton energy. The longest-wavelength emission occurs near the edges of the islands, at locations that also tend to exhibit high PL intensity. If regions of stronger exciton binding (and hence lower-energy PL emission) correspond to minima in an effective potential for excitons, then the red-shifted regions near the island edges can be

dx.doi.org/10.1021/nl3026357 | Nano Lett. 2013, 13, 3447–3454

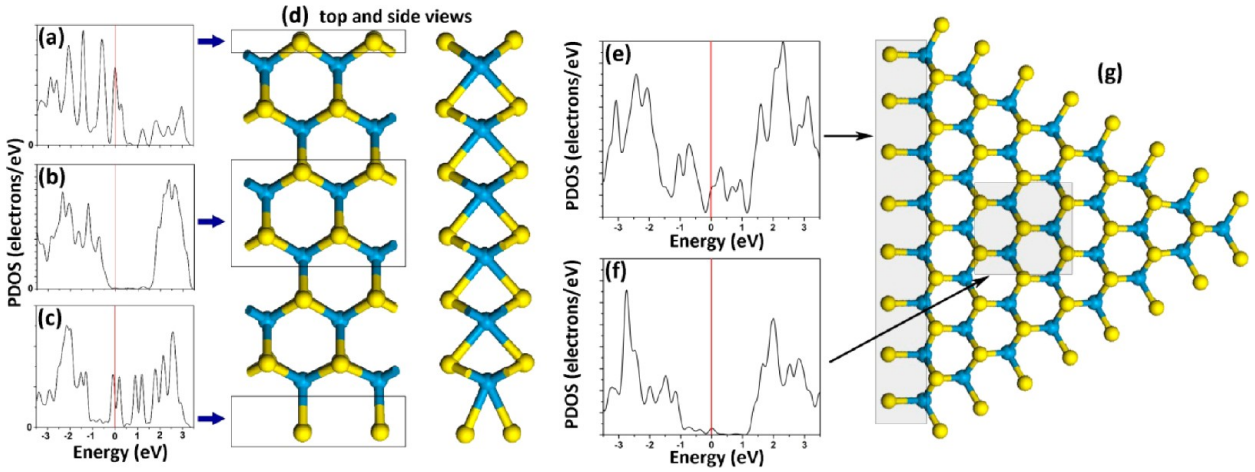

Figure 6. (a, b, and c) PDOS adding the alpha (up) and beta (down) spins of three different WS_2 nanorribbon regions: (a) Bare sulfur zigzag edge. (b) Central region with infinite monolayer features. (c) Fully sulfur passivated tungsten edge. (d) Model consisting of a double unit cell used in the calculations. PDOS (as a sum of the alpha and beta spins) of a triangular cluster with zigzag edges fully passivated with sulfur. (e) PDOS at the sulfur−tungsten edge. (f) PDOS at the central region of the island showing infinite monolayer features. (g) Model showing shaded regions where the PDOS has been considered.

interpreted as accumulation points for excitons, consistent with the higher PL intensity in these regions. Lattice defects such as edge dipoles, impurities, or vacancies could localize excitons and thereby create inhomogeneities in the exciton binding energy.

The most striking result is the position dependence of the PL intensity even within the monolayer regions. Figure 5i reveals that the $I_{PL}/I_{A_{1g}}$ ratio can vary from 36 at the interior of a monolayer platelet (location P2) to 880 near the edge (location P5). Splendiani et al.[8] reported only a 3-fold enhancement in mechanically exfoliated MoS_2 monolayers. For comparison, we have also synthesized monolayer MoS_2 triangular islands and these exhibit weak PL. For small triangular WS_2 islands (shown in Figure 5e) the maximum PL intensity also occurs close to the borders and the vertices of the islands. The mechanism for these hot spots in the PL signal is still unknown, but it may be related to the PL redshift near the island edges (Figure 5g and h), as discussed above. In bulk 3D semiconductors (e.g., Si and GaAs) shallow impurities can bind free excitons. In our case the PL enhancement is clearly related to specific edge geometries. Using an ultrasharp tungsten needle (OMNI Probe), we scratched two parallel lines in a triangular WS_2 island as shown in Figure 5j; the edges created mechanically do *not* show any significant PL enhancement (Figure 5k and l). This result suggests that the edge structure and chemistry of as-grown monolayer WS_2 islands are crucial for localized PL enhancement. The actual mechanism leading to the edge-enhanced PL is still to be determined and will require understanding the dynamics of 2D excitons and their interaction with local fields near the edges.

Besides the modified optical behavior observed in this work, many reports have demonstrated that edges in two-dimensional clusters play a significant role in modifying the local physicochemical properties of the material. For instance, diverse edge passivation in metal dichalcogenides could produce different spins states that change the edge magnetic properties.[35] Furthermore, recent first-principles calculations have indicated that a high spin density could be localized surrounding metal vacancies in similar types of metal dichalcogenides.[11] Enhanced catalytic activity has been also correlated with the density of edges sites in MoS_2 2D clusters.[36] These unusual edge behaviors have inspired us to further investigate through first principles calculations the electronic properties of finite WS_2 monolayers.

We carried out DFT spin polarized simulations on individual triangular zigzag-edge WS_2 clusters ($S_{84}W_{28}$ and $S_{104}W_{36}$) and WS_2 (6-zigzag) nanoribbons (see Supporting Information) since this type of edge has been identified through electron diffraction of our samples. A zigzag edge, preserving the stoichiometry, can terminate in either sulfur or tungsten. These two possibilities can be studied within a single WS_2 zigzag nanoribbon (see Figure 6 a−d). Due to the high reactivity of bare tungsten edges, they should be passivated with the atomic species present in the chamber, such as sulfur and oxygen (this last in much lower concentration): sulfur, because of its high content in our experiment, and oxygen since the precursor material is WO_3. It is noteworthy that sulfur passivation has been studied in zigzag MoS_2 triangular islands using STM, identifying states at the Fermi level at the edges.[23,37] Taking this into account, we have obtained the partial density of states (PDOS) from bulk-like and edge regions of the WS_2 nanoribbons (Figure 6 a−d) with sulfur and oxygen passivation (see Supporting Information) and also from triangular WS_2 clusters (Figure 6 e−g). In both cases (WS_2 triangular islands and WS_2 nanoribbons), the interiors rapidly develop semiconducting behavior similar to that of a full monolayer, with a band gap around 2 eV, consistent with the experimental observation of PL. The edges in each case examined (bare sulfur, bare tungsten, sulfur, or oxygen passivated tungsten) support edge-localized states at the Fermi level. For the oxygen-terminated tungsten edge, a chemisorbed termination with atomic oxygen in a bonding geometry similar to that of WO_3 (and a lower density of states near the Fermi level) is preferred over physisorbed molecular oxygen by 0.3 eV per 40-atom cell (see Supporting Information). The detailed behavior of the edge states, including possible magnetism and more complex adsorbed species, will be published elsewhere.

In summary, we have reported the first successful synthesis of individual (S−W−S) monolayers of WS_2. We also established a Raman signature for individual WS_2 monolayers. The observation of room-temperature PL in a WS_2 monolayer is

dx.doi.org/10.1021/nl3026357 | *Nano Lett.* 2013, 13, 3447−3454

reported here for the first time. This photoluminescent behavior is supported by the transition of the system from indirect-gap behavior in the bulk to direct-gap behavior in monolayers, as predicted by our calculations. Moreover, the PL signal undergoes an extraordinary enhancement toward the edges (and corners) of our triangular platelets. Our observations thus motivate future work to engineer structures to tailor the optoelectronic response of monolayers of metal dichalcogenides, both to elucidate the fundamental mechanisms of edge-enhanced PL and also to develop potential future nano-optoelectronic devices. The fact that this material can be synthesized on SiO_2/Si substrates, following a simple and reproducible route, opens up numerous possibilities for 2D device fabrication. The electronic properties of the infinite 2D monolayer, the bulk (i.e. multilayer), as well as different kinds of edge passivation in finite systems were also investigated by first-principles calculations.

Materials and Methods. *Synthesis.* WO_3 thin films (5−20 Å) were thermally deposited on SiO_2/Si substrates in a high-vacuum chamber (10^{-5}−10^{-6} Torr). Prior to thermal deposition, a SiO_2/Si wafer was diced into 1 cm^2 pieces, washed in an ultrasonic bath with acetone and isopropanol (50/50), and blow dried with UHP nitrogen gas. Subsequently, the films were transferred into a quartz tube reactor. During the sulfurization of the WO_3 films, the samples were kept at 800 °C for 30 min under an argon flow, and S vapors were generated from S powders placed upstream at a lower temperature region (~250 °C) which was controlled independently. The sulfurization experiments were conducted under an Ar flow ranging from 100 to 500 sccm and at atmospheric pressure.

For the TEM observations, we transferred as-grown WS_2 islands onto gold Quantifoil TEM grids (from SPI), which have a polymer thin film with 2 μm periodic holes. The WS_2 islands were released from the original Si/SiO_2 wafer by the etching effect of a KOH 15 M solution. A first approach[38] consisted on coating the wafer with a PMMA solution (495 000) by spin coating, with a speed of 3000 rpm, for 30 s. The polymer was then allowed to cure overnight at room temperature. The edge of the wafer was marked with a sharp blade to expose the Si/SiO_2 surface, and the wafer was subsequently immersed in the KOH 15 M solution. The PMMA/WS_2 film was released by the effect of the caustic solution and was fished out with the TEM grid. The TEM grid was placed on absorbent paper and thoroughly washed with deionized water. Finally, the PMMA was dissolved with acetone droplets. A direct PMMA-free approach was also followed.[39] A TEM grid was placed on the Si/SiO_2 wafer containing the WS_2 islands. One drop of IPA was allowed to dry on the TEM grid. After 10 min, the wafer was immersed in the KOH 15 M solution. The grid was released and placed on absorber paper and was washed thoroughly with deionized water.

Characterization. The WO_3 films were characterized by Raman and PL spectroscopies, performed in a Renishaw inVia confocal microscope-based Raman spectrometer using the 488 nm laser line as the excitation wavelength. The spectra were acquired with a maximum laser power of 0.028 mW. The spectra were collected in back-scattering geometry; for the maps acquisition both the excitation and collection optics remained fixed while the sample was moved in x and y. PL mappings were conducted under an inert atmosphere and in air with no significant difference. The 520 cm^{-1} phonon mode from the silicon substrate was used for calibration. High-resolution transmission electron microscopy (HRTEM) was carried out in a JEOL 2010F with an accelerating voltage of 200 kV, field-emission source, ultra-high-resolution pole piece (Cs = 0.5 mm), 1.9 Å Scherzer limit, and equipped with an energy dispersive X-ray (EDX) spectrometer. Two different microscopes were used in our experiments: LEO 1530 FESEM and FEI NanoSEM 630 FESEM. Noncontact atomic force microscopy was performed in a MFP-3D-SA made by Asylum Research.

Theoretical Modeling. Density functional theory (DFT) spin-polarized simulations on individual triangular zigzag WS_2-like clusters with sizes $n = 7$ ($S_{84}W_{28}$) and $n = 8$ ($S_{104}W_{36}$) were carried out using the DMOL3 code as implemented in Materials Studio. The general gradient approximation (GGA) was used as exchange-correlation potential and the Perdue-Burke-Ernzerhof (PBE) functional with an atomic cutoff radius of 4.5 Å.[40,41] The clusters were optimized to reach a convergence energy tolerance of 2×10^{-5} Ha/atom with a maximum force per atom of 0.004 Ha/Å. Additional calculations in which the clusters were put in a box have been carried out, with distances between clusters of 35 Å of vacuum to reduce interactions among them.

WS_2 nanoribbons were simulated using a plane wave code as implemented in CASTEP,[42] considering single and double supercells ($2 \times 1 \times 1$ to allow reconstruction at the edges) under GGA-PBE with a Monkhorst-Pack k-point grid with $9 \times 1 \times 1$ k-points and a plane wave basis cutoff of 500 eV; optimizing the geometry until the total energy reaches 2×10^{-5} eV/atom and the maximum force per atom exhibits values less than 0.05 eV/Å.

For the bulk WS_2 and single-layer calculations, the CASTEP[42] plane wave code was used under GGA-PBE considering a Monkhorst−Pack grid with $9 \times 9 \times 1$ k-points and a plane wave basis cutoff of 500 eV; optimizing the geometry until the total energy reaches 2×10^{-5} eV/atom and the maximum force per atom exhibits values less than 0.05 eV/Å.

■ ASSOCIATED CONTENT

Supporting Information

Optical contrast of monolayered WS_2 on Si/SiO_2 substrates; PL and Raman from the WO_x precursors; position dependence of the WS_2 monolayers PL full width at half maximum (FWHM) and PL integrated intensity; comparison of the PL signal and FWHM for WS_2 and MoS_2; and additional first-principles calculations for different edge passivation. This material is available free of charge via the Internet at http://pubs.acs.org.

■ AUTHOR INFORMATION

Present Address

[‖]Department of Physics and Astronomy, University of Louisville, Louisville, Kentucky 40292, United States.

Notes

The authors declare no competing financial interest.

[⊥]On leave from Advanced Materials Department, IPICYT, Camino a Presa San Jose 2055, Col. Lomas 4a Sección, San Luis Potosí, México.

■ ACKNOWLEDGMENTS

This work is supported by the U.S. Army Research Office MURI grant W911NF-11-1-0362. Supported in part by the Materials Simulation Center of the Materials Research Institute, the Research Computing and Cyberinfrastructure unit of

Information Technology Services and Penn-State Center for Nanoscale Science. M.T. and V.H.C. also acknowledge support from the Penn State Center for Nanoscale Science for seed grant on 2-D Layered Materials (DMR-0820404). This publication was also supported by the Pennsylvania State University Materials Research Institute Nanofabrication Lab and the National Science Foundation Cooperative Agreement No. ECS-0335765. Other electron microscopy characterization facilities within the Materials Research Institute at the Pennsylvania State University were also used for this research. Specific author contributions are as follows: M.T. and H.R.G. conceived the project ideas. H.R.G. and N.P.L. worked together to develop the synthesis approach and obtained the WS_2 samples. H.R.G. and A.B. performed optical spectroscopy (Raman and PL) and data analysis. H.R.G. performed TEM measurements and analysis. N.P.L. and A.L.E. provided SEM images. A.L.E. and R.L. worked on the films transfers to a different substrate. B.W. performed AFM measurements. H.T. and F.L.U. made first principles theoretical calculations. H.R.G., H.T., and M.T. wrote the manuscript. V.H.C. contributed with valuable ideas, discussions, and manuscript revision. All of the authors discussed the results and commented the manuscript. We are grateful to Dr. Rodolfo Cruz-Silva for recording the fluorescence image of the WS_2 islands used as a background for the cover of this issue.

REFERENCES

(1) Geim, A. K.; Novoselov, K. S. The rise of graphene. *Nat. Mater.* **2007**, *6*, 183−191.
(2) Jin, C. H.; Lin, F.; Suenaga, K.; Iijima, S. Fabrication of a Freestanding Boron Nitride Single Layer and Its Defect Assignments. *Phys. Rev. Lett.* **2009**, *102*, 195505.
(3) Ci, L.; et al. Atomic layers of hybridized boron nitride and graphene domains. *Nat. Mater.* **2010**, *9*, 430−435.
(4) Novoselov, K. S.; et al. Two-dimensional gas of massless Dirac fermions in graphene. *Nature* **2005**, *438*, 197−200.
(5) Zhang, Y. B.; Tan, Y. W.; Stormer, H. L.; Kim, P. Experimental observation of the quantum Hall effect and Berry's phase in graphene. *Nature* **2005**, *438*, 201−204.
(6) Castro Neto, A. H.; Guinea, F.; Peres, N. M. R.; Novoselov, K. S.; Geim, A. K. The electronic properties of graphene. *Rev. Mod. Phys.* **2009**, *81*, 109−162.
(7) Mak, K. F.; Lee, C.; Hone, J.; Shan, J.; Heinz, T. F. Atomically Thin MoS(2): A New Direct-Gap Semiconductor. *Phys. Rev. Lett.* **2010**, *105*, 136805.
(8) Splendiani, A.; et al. Emerging Photoluminescence in Monolayer MoS(2). *Nano Lett.* **2010**, *10*, 1271−1275.
(9) Eda, G.; et al. Photoluminescence from Chemically Exfoliated MoS(2). *Nano Lett.* **2011**, *11*, 5111−5116.
(10) Albe, K.; Klein, A. Density-functional-theory calculations of electronic band structure of single-crystal and single-layer WS2. *Phys. Rev. B* **2002**, *66*, 073413.
(11) Ma, Y. D.; et al. Electronic and magnetic properties of perfect, vacancy-doped, and nonmetal adsorbed MoSe(2), MoTe(2) and WS(2) monolayers. *Phys. Chem. Chem. Phys.* **2011**, *13*, 15546−15553.
(12) Ding, Y.; et al. First principles study of structural, vibrational and electronic properties of graphene-like MX(2) (M = Mo, Nb, W, Ta; X = S, Se, Te) monolayers. *J. Phys.: Condens. Matter* **2011**, *406*, 2254−2260.
(13) Margulis, L.; Salitra, G.; Tenne, R.; Talianker, M. Nested Fullerene-Like Structures. *Nature* **1993**, *365*, 113−114.
(14) Frey, G. L.; Tenne, R.; Matthews, M. J.; Dresselhaus, M. S.; Dresselhaus, G. Optical properties of MS_2 (M = Mo, W) inorganic fullerene-like and nanotube material optical absorption and resonance Raman measurements. *J. Mater. Res.* **1998**, *13*, 2412−2417.
(15) Tenne, R.; Margulis, L.; Genut, M.; Hodes, G. Polyhedral and Cylindrical Structures of Tungsten Disulfide. *Nature* **1992**, *360*, 444−446.
(16) Rapoport, L.; et al. Hollow nanoparticles of WS_2 as potential solid-state lubricants. *Nature* **1997**, *387*, 791−793.
(17) Remskar, M.; et al. New crystal structures of WS_2: Microtubes, ribbons, and ropes. *Adv. Mater.* **1998**, *10*, 246−249.
(18) Zhu, Y. Q.; et al. Nb-doped WS(2) nanotubes. *Chem. Phys. Lett.* **2001**, *342*, 15−21.
(19) Liu, K. K.; et al. Growth of Large-Area and Highly Crystalline MoS_2 Thin Layers on Insulating Substrates. *Nano Lett.* **2012**, *12*, 1538−1544.
(20) Lee, C.; et al. Anomalous Lattice Vibrations of Single- and Few-Layer MoS(2). *ACS Nano* **2010**, *4*, 2695−2700.
(21) Matte, H. S. S. R.; et al. MoS(2) and WS(2) Analogues of Graphene. *Angew. Chem., Int. Ed.* **2010**, *49*, 4059−4062.
(22) Coleman, J. N.; et al. Two-Dimensional Nanosheets Produced by Liquid Exfoliation of Layered Materials. *Science* **2011**, *331*, 568−571.
(23) Lauritsen, J. V.; et al. Size-dependent structure of MoS(2) nanocrystals. *Nat. Nanotechnol.* **2007**, *2*, 53−58.
(24) Zhan, Y.; Liu, Z.; Najmaei, S.; Ajayan, P. M.; J., L. Large-Area Vapor-Phase Growth and Characterization of MoS2 Atomic Layers on a SiO_2 Substrate. *Small* **2012**, *8*, 966−971.
(25) Lee, Y. H.; et al. Synthesis of Large-Area MoS_2 Atomic Layers with Chemical Vapor Deposition. *Adv. Mater.* **2012**, *24*, 2320−2325.
(26) Yin, Z. Y.; et al. Single-Layer MoS2 Phototransistors. *ACS Nano* **2012**, *6*, 74−80.
(27) Radisavljevic, B.; Radenovic, A.; Brivio, J.; Giacometti, V.; Kis, A. Single-layer MoS(2) transistors. *Nat. Nanotechnol.* **2011**, *6*, 147−150.
(28) Schutte, W. J.; Deboer, J. L.; Jellinek, F. Crystal-Structures of Tungsten Disulfide and Diselenide. *J. Solid State Chem.* **1987**, *70*, 207−209.
(29) Ballif, C.; et al. Preparation and characterization of highly oriented, photoconducting WS_2 thin films. *Appl. Phys. A: Mater. Sci. Process.* **1996**, *62*, 543−546.
(30) Frey, G. L.; Elani, S.; Homyonfer, M.; Feldman, Y.; Tenne, R. Optical-absorption spectra of inorganic fullerenelike MS_2 (M = Mo, W). *Phys. Rev. B* **1998**, *57*, 6666−6671.
(31) Brothers, A. D.; Brungardt, J. B. Excitons in WS_2 Films - Pressure and Temperature Effects. *Phys. Status Solidi B* **1979**, *91*, 675−679.
(32) Gupta, A.; Chen, G.; Joshi, P.; Tadigadapa, S.; Eklund, P. C. Raman scattering from high-frequency phonons in supported n-graphene layer films. *Nano Lett.* **2006**, *6*, 2667−2673.
(33) Bertram, N.; et al. Nanoplatelets made from MoS_2 and WS_2. *Chem. Phys. Lett.* **2006**, *418*, 36−39.
(34) Molina-Sanchez, A.; Wirtz, L. Phonons in single-layer and few-layer MoS_2 and WS_2. *Phys. Rev. B* **2011**, *84*, 155413.
(35) Botello-Mendez, A. R.; Lopez-Urias, F.; Terrones, M.; Terrones, H. Metallic and ferromagnetic edges in molybdenum disulfide nanoribbons. *Nanotechnology* **2009**, *20*, 325703.
(36) Jaramillo, T. F.; et al. Identification of active edge sites for electrochemical H-2 evolution from MoS_2 nanocatalysts. *Science* **2007**, *317*, 100−102.
(37) Bollinger, M. V. et al. One-dimensional metallic edge states in MoS_2. *Phys. Rev. Lett. 87* (**2001**).
(38) Reina, A.; et al. Large Area, Few-Layer Graphene Films on Arbitrary Substrates by Chemical Vapor Deposition. *Nano Lett.* **2009**, *9*, 30−35.
(39) Regan, W.; et al. A direct transfer of layer-area graphene. *Appl. Phys. Lett.* **2010**, *96*, 113102.
(40) Delley, B. An All-Electron Numerical-Method for Solving the Local Density Functional for Polyatomic-Molecules. *J. Chem. Phys.* **1990**, *92*, 508−517.
(41) Delley, B. From molecules to solids with the DMol(3) approach. *J. Chem. Phys.* **2000**, *113*, 7756−7764.
(42) Clark, S. J.; et al. First principles methods using CASTEP. *Z. Kristallogr.* **2005**, *220*, 567−570.